THE EFFECT OF PLY BLOCKING ON NEAR-EDGE IMPACT DAMAGE MECHANISMS

S. Hua[1], N. Dubary[2], C. Bouvet[2], A.T. Rhead[1*]
[1] Materials and Structures Research Centre, University of Bath, Bath, UK,
[2]Institut Clément Ader, Institut Supérieur de l'Aéronautique et de l'Espace, Toulouse, France
* Corresponding author (A.T.Rhead@bath.ac.uk)

Keywords: *impact damage, damage tolerance, X-ray CT, FEA*

ABSTRACT

Out-of-plane impact near the edge of composite plates has received little attention in the research literature but is a recognized damage mode for aerospace structures and can lead to significant reductions in compressive strength. In this paper, a combined high fidelity Discrete Ply Finite Element Analysis (DPFEA) and quasi-static in-situ X-ray Computed Tomography (XRCT) approach is used to provide insight into the processes driving damage formation in near edge impact of a $[(\pm45)_3(0_3/90)_2/0_2]_S$ laminate. Comparison of DPFEA and XRCT results highlight the significance of $0_n/90$ interfaces in the development of the most extensive delaminations. Ply blocking is seen to contain damage to the inner 50% of plies in the laminate. Discrepancies are seen between the XRCT and DPFEA results as a consequence of the extent of numerical modelling of the experimental boundary conditions and the need for further consideration of the effect of compression on fracture.

1. INTRODUCTION

Owing to the significant reduction in residual strength that it can cause, both academia and the aerospace industry have undertaken extensive research into impact damage of CFRP laminates [1-14]. Of this damage, Barely Visible Impact Damage (BVID) is particularly dangerous because it is difficult to detect in service. Despite this research effort and multiple competing theories to describe damage formation, there is currently limited understanding of the mechanisms that determine impact damage morphology in general and near edge impact in particular [6,7,10-13]. This is partially a consequence of the dynamic nature of impact and partially a consequence of the comparatively long scan-times required by NDE techniques capable of inspecting internal damage, e.g C-scan and X-ray Computed Tomography (XRCT). As such NDE of damaged laminates has previously been constrained to post-test analysis of unloaded coupons [1,2,15]. As delaminations and intra-ply cracks close when load is removed, some information is lost in standard NDE tests making it difficult to identify mechanisms that shape damage morphology. However, at the low velocities at which BVID typically forms, laminate response is dominated by the lowest mode shape implying that load, deflection and hence, the strain are effectively in the same phase. As such, quasi-static loading is a good approximation of the low velocity impacts that typically produce BVID [3-5]. In this paper, a novel rig for in-situ X-ray Computed Tomography (XRCT) imaging of laminates under out-of-plane near edge indentation is used to capture quasi-static impact damage progression through incremental scanning and loading of a $[(\pm45)_3(0_3/90)_2/0_2]_S$. laminate.

Observations of experimental damage progression with increasing increments will be compared with a Discrete Ply Finite Element Analysis (DPFEA) [16]. Previous validation of the DPFEA technique has been mainly restricted to post-test static NDE and low-speed in-situ thermal NDE. However, DPFEA has previously successfully used interface elements to capture the interaction of intraply cracking and delamination following on-edge and out-of-plane impact and CAI testing [6,17]. Here the DPFEA will be used to investigate failure mechanisms in near edge impact. Capture of internal quasi-static damage development will allow for further refinement of FEA damage processes and will guide further development.

2. EXPERIMENTAL METHOD

2.1 Coupon design and manufacture

An approximately semi-circular coupon was manufactured to allow investigation of out-of-plane near edge impact. The coupon has a 32 ply stacking sequence $[(\pm45)_3(0_3/90)_2/0_2]_S$ and geometry defined in Fig. 1(a). All samples were manufactured from M21/T800, unidirectional CFRP prepreg with ply thickness 0.25mm resulting in a full laminate thickness of 8mm.

2.2 Loading stage design and operation

The in-situ XRCT loading rig is shown in Fig. 1(b). A loading screw is used to apply incremental increases in indenter displacement. Each displacement is held for 255 minutes, the time required to XRCT scan the sample. In order to capture the order of damage progression, the coupon was scanned under zero load and then at multiple indentor displacmeents with damage being detecte at dispalcements of 3.1mm, 4.2mm and 5.4mm; displacement being measured using measurements of the displacement of the loading screw relative to the rig surface. It is noted that no evidence of rigid body movement of the sample relative to its fixture was noted during scanning and that the loading stage remained locked in position in the XRCT scanner throughout all applications of load. Displacement was halted after either audible cracking or after 1mm displacement steps. XRCT scans were taken using a Nikon XT H 225 ST CT scanner with a Tungsten target and Perkin Elmer 1620 16-bit, 2000 by 2000 pixel detector. The system has a 225kV microfocus source with a minimum 3μm spot size. Between 2033 and 3141 projections (with 4-8 averages per projection) were taken per scan with each projection being a composite of the average of 4 images. Images were taken with 708ms exposures under x-ray conditions of 155kV and 150 μA.

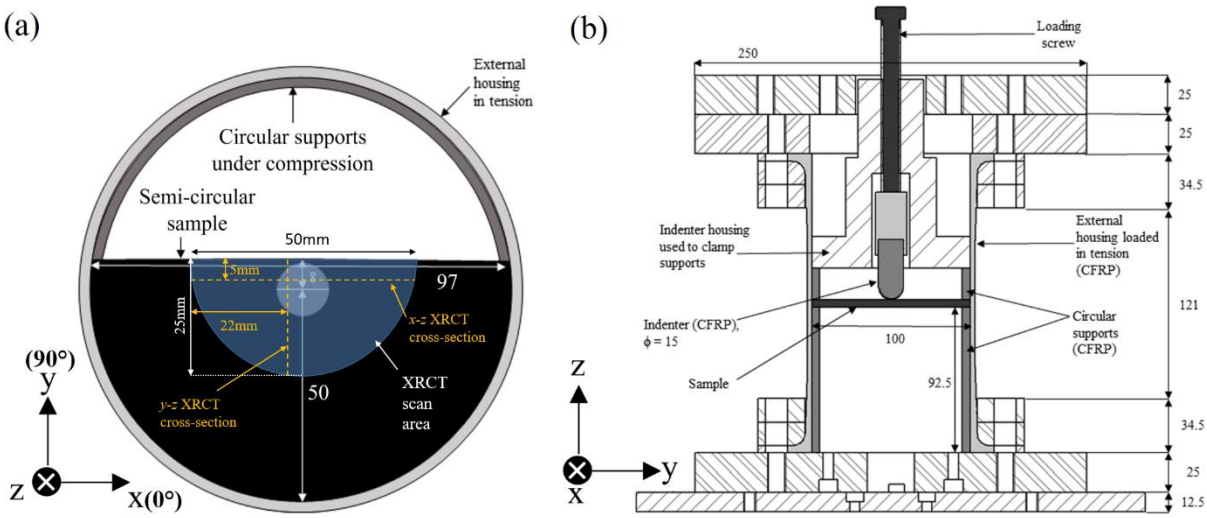

Figure 1: (a) *x-y* plane cross sectional view of the jig showing supports, indenter and coupon; (b) *z-y* cross-section of the load stage showing coupon placement and load stage construction.

3. DISCRETE PLY FINITE ELEMENT ANALYSIS

DPFEA has already been described in several papers [6,16-19] and retains the same characteristics as Achard et al. for open-hole tension test modelling [18]. In particular, core features such as mesh construction and behavior law are unchanged. Material properties used in the DPFEA modelling are as follows: density ρ =1600 x 10^{-12} tons/mm^3, tensile Young's modulus in fibre direction $E_{11,tension}$ = 165GPa, compressive Young's modulus in fibre direction $E_{11,compression}$ = 115GPa, transverse Young's modulus E_{22} = 7.7GPa, shear modulus G_{12} = 4.75GPa, Poisson's ratio ν_{12} = 0.3, transverse failure stress S_n = 60MPa, shear failure stress S_t = 110MPa, crushing stress σ_0 = 250MPa, fibre failure strain in tension ε_{0t} = 0.017, fibre failure strain in compression ε_{0c} = -0.0125, Mode I fracture strain energy

release rate 0.5 N/mm, Mode II fracture strain energy release rate 1.6 N/mm, strain energy release rate for tensile fibre fracture G_{ft} =100N/mm, strain energy release rate for compressive fibre fracture G_{fc} = 40N/mm, stiffness of delamination interfaces R_D = 500000 MPa/mm and stiffness of intraply cracking interfaces R_f = 1000000 MPa/mm.

3.1 Mesh construction

DPFEA captures the three major composite laminate failure modes: intra-ply fibre failure, intra-ply matrix cracking and inter-ply delamination. 3D volume elements (C3D8) are used to model fibre fracture and plies are separated by zero-thickness cohesive elements (COH3D8) to represent delamination and matrix cracking, see Fig. 2(a). DPFEA uses four nodes at each point to naturally capture cracking/delamination coupling; two to model matrix cracking of the upper ply, two to model matrix cracking of the lower ply and the two pairs are connected by delamination elements, see Fig 2(b). Use of parallelogram-shaped elements for +/- 45 ° plies is necessary to ensure node alignment.

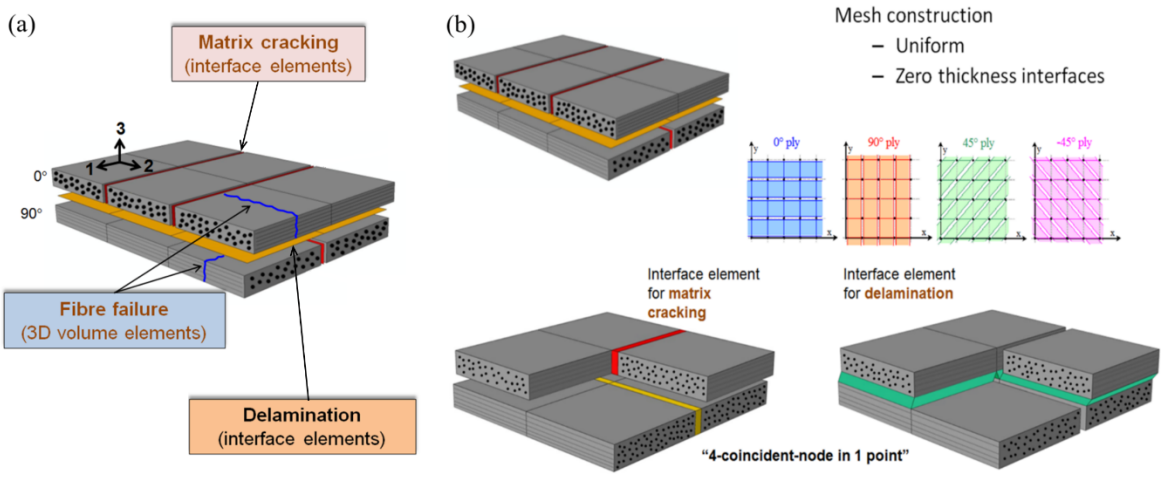

Figure 2: (a) DPFEA damage failure modes (b) Mesh specificities of the DPFEA [18].

An element size of 1mm is used in the in-plane directions, and between 0.25mm and 1mm in the out-of-plane direction depending on the number of consecutive plies of the same orientation (between 1 and 4 plies 0.25mm-thick). The in-plane size of elements is justified by work by Li and Chen [20] who numerically determined the ratio of minimum distance between transverse cracks and ply thickness to be 1.53 and 1.60 for HS300/ET223 and T300/NY9200Z materials respectively. Crack saturation distance is significantly more dependent on the thickness of the cracked neighbouring ply stiffness.

3.2 Modelling of matrix cracking

Figure 3 (a) shows the DPFEA approach to intra-ply cracking. To prevent the occurrence of stress concentrations, failure criterion calculations are not carried out within the interface element itself but instead in the neighbouring volume elements i.e. if the Hashin criterion,

$$\left(\frac{\langle\sigma_t\rangle^+}{Y^T}\right)^2 + \frac{\tau_{lt}^{\ 2} + \tau_{tz}^{\ 2}}{\left(S^L\right)^2} \leq 1 \qquad (1)$$

is met in either one (E1) or the other (E2) volume elements in Fig. 3 then, the stiffness of the interface (I1) (initially of 10^6 MPa/mm) is set to zero. Here σ_t is the transverse stress, τ_{lt} and τ_{tz} the shear stresses in the (*lt*) and (*tz*) planes, $< >^+$is the positive value, Y^T is the transverse failure stress and S^L is the shear failure stress of the ply. Use of interface elements to simulate matrix cracking indicates only through-

the-ply-cracks are taken into account in this method. The implication of this method is that matrix cracks propagate fast in a thin ply and therefore diffuse damage should not be considered.

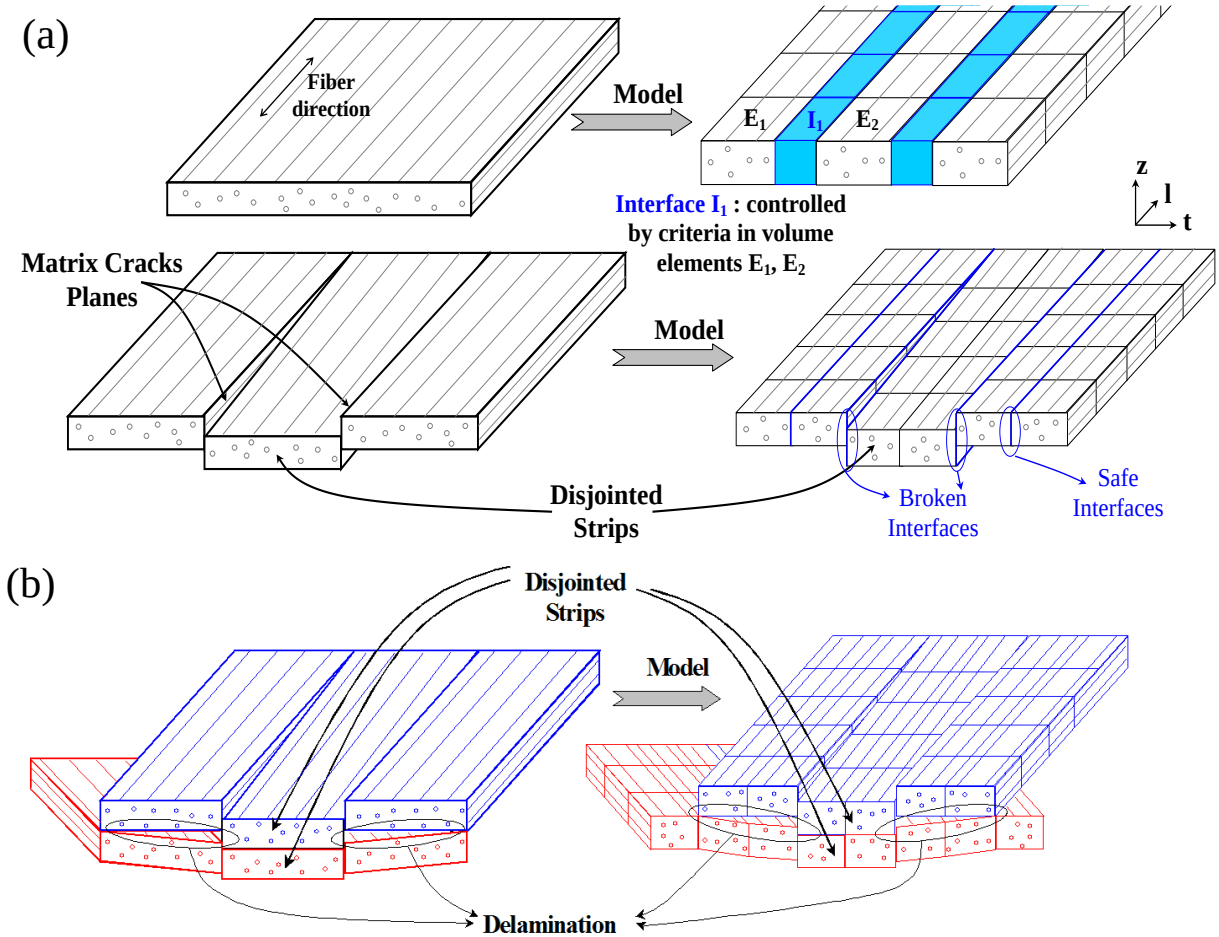

Figure 3: Discrete Ply Modelling of (a) matrix failure and (b) delamination [21].

3.3. Modelling of fibre failure

As described in Fig. 4(a), fibre failure is modelled continuously; a break is initiated when the fibre strain reaches the failure strain ε_0^T. Propagation is included in the model using the critical energy restitution rate $G_{Ic}^{fibre,t}$, fibre keeps lengthening until consistent energy has been dissipated (2). The stiffness of the affected volume elements is gradually reduced until fibre strain reaches ε_I^T.

$$\int_V \left(\int_0^{\varepsilon_I^T} \sigma_l . d\varepsilon_l \right) . dV = S.G_{Ic}^{fibre,t} \tag{2}$$

Where σ_l (ε_l) is the longitudinal stress (strain), V (S) is the volume (section) of the element, ε_I^T is the strain of total degradation of the fibre stiffness (Fig. 4) and $G_{Ic}^{fibre,t}$ is the energy release rate in opening mode in the direction of the fibres.

First order volume elements have been chosen to ensure correct bending behavior is correctly described with only one element in the ply thickness. Indeed, two nodes along the thickness direction of the ply are enough to describe affine strain variation within the element. A communication law between the 8 integration points is used to ensure the correct amount of energy is dissipated on average per element. Mesh independence is ascertained by the characteristic length used in the model which is the volume element length. A constant energy is released per unit area, independently of the element length. This type of approach has first been used by Bazant et al. [22] to model concrete failure.

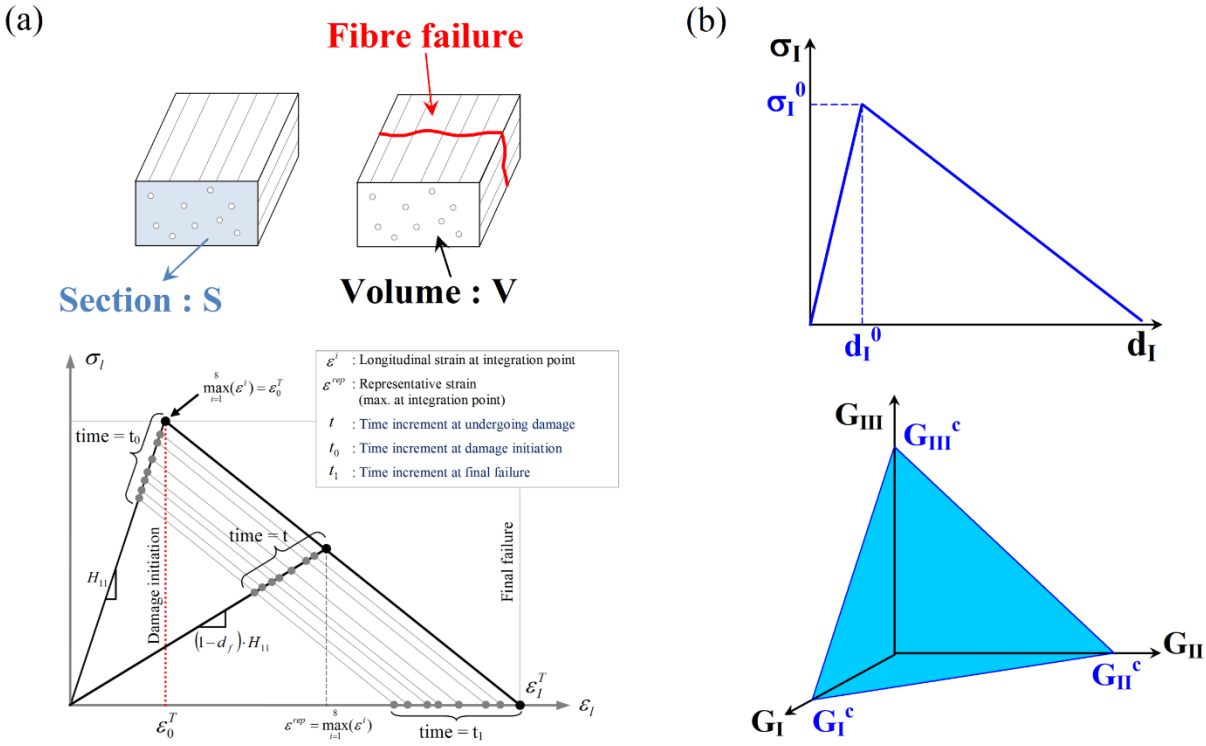

Figure 4: (a) DPFEA Modelling of fibre failure [18] and (b) DPFEA delamination behaviour law [21].

It is noted that other techniques exist to build mesh independent numerical models. Models based on Cosserat theory [23], non-local models [24], delay effect techniques [25], and combined approaches such as the one developed by Marcin et al. [26] also permit regularization to reduce mesh dependency.

3.4 Modelling of delamination

Like matrix cracking, delamination is modelled using cohesive interfaces, see Fig. 3(b). The main difference is that energy is dissipated solely by delamination. Otherwise, the energy dissipated by matrix cracking would be dependent on mesh density. However, energy spent in matrix cracking is still taken into account. This is because experimental methods for determining critical energy release rates for delamination, such as the double cantilever beam test, include multiple modes of damage and thus include most of the energy dissipated through matrix cracking in addition to energy derived from delamination. Delamination modelling is based on fracture mechanics with a linear softening stress versus displacement behaviour law, see Fig. 4(b). The shape of the unloading curve has, according to Hellweg [27], a very moderate effect on the overall behavior. For instance, a mode I delamination is initiated when the distance between nodes reaches a critical distance d_I^0. Degradation of the stiffness in Mode I is then activated and ends when the critical energy release rate is dissipated. To capture the different modes of propagation (I, II and III), equivalent distance and critical energy release rate are determined, see Fig. 3(b).

3.5 Mesh description of experimental problem

Figure 5 shows the DPFEA mesh approximating the experimental set up in Fig. 1. The indenter consists of analytical rigid surface and the contact is simulated using a penalty contact algorithm and a friction coefficient of 0.1. The supporting boundary is modelled as offering either simple or clamped support to the coupon and consists of analytical rigid surfaces (same contact as this one with indenter). The coupon consists of about 100000 volumic elements (C3D8), about 100000 delamination interface elements and about 100000 matrix cracking interface elements, as described in Sections 3.1-3.4. Indeed, 21 solid elements and 20 delamination interfaces are necessary through the laminate thickness (each group of consecutive plies of the same orientation are meshed with one volume element).

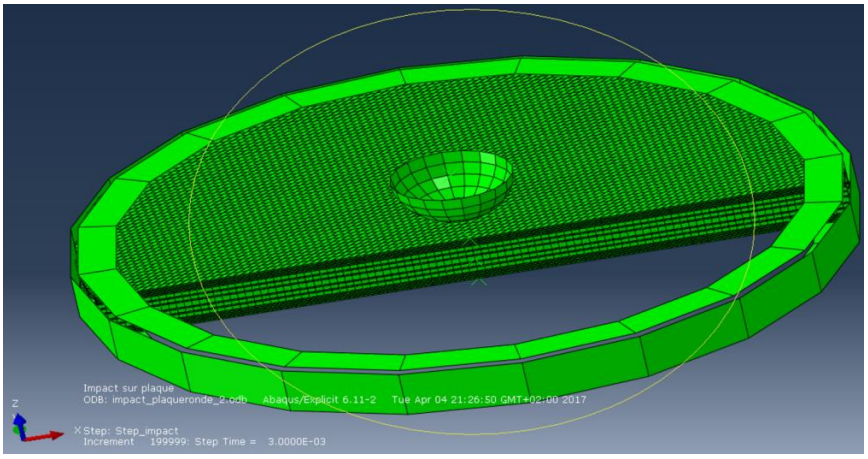

Figure 5: DPFEA mesh showing the coupon, indenter and supports.

5. RESULTS

Figure 6 compares the load vs. displacement response of the coupon in the experiment with DPFEA results for clamped and simply supported curved boundary; the straight boundary is free in both cases. Highlighted points of the load-displacement curve (Fig. 6) correlate with XRCT scans where growth of damage was detected and are related to cross-sectional images in Figs. 7-9. Figure 1(a) displays the locations of cross-sections in the *x-y* plane. Figures 7 and 8 show the progression of damage with increasing load at highlighted points on Fig. 6 and for both test and DPFEA. Figs. 8(a), (c) and (e) are *y-z* cross-sections of the XRCT scan taken of the in-situ indentation and Figs. 8(b), (d) and (f) are the respective numerical comparisons. Similarly Figure 7 gives *x-z* cross-sectional images as per Fig. 1(a). Doubling of cracks in Figs. 7(d) and 8(c) were the consequence of defective operation of the XRCT turntable but still offer valuable insight into the extent of delamination propagation.

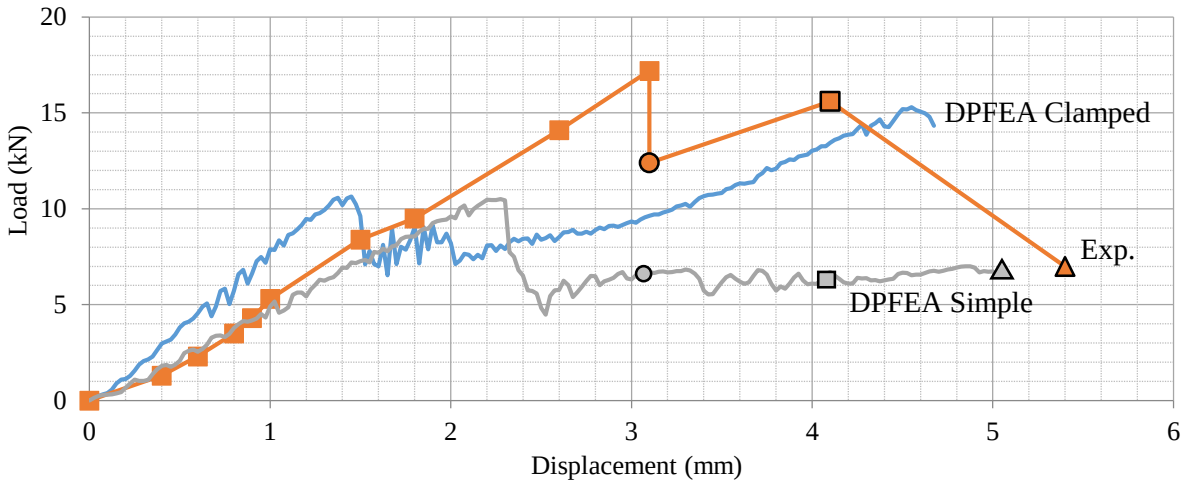

Figure 6: Experimental and DPFEA (clamped and simple supports) Load vs. Displacement for quasi-static indentation of $[(\pm45)_3(0_3/90)_2/0_2]_S$ laminate.

In Figs 7(f) and 8(e) damage in the experimental images is colourised (based on absolute *z* position) to better indicate the extent and interconnection of damage at the final loading stage. In Figure 9 all the laminate material has been made transparent leaving behind just the colourised damage regions. Figure 9 shows the areal extent of damage as captured by XRCT and DPFEA at 3.1mm, 4.2mm (DPFEA only) and 5.4mm. The extent of damage is shown from both the impact and non-impact surfaces. Note that DPFEA images show the extent of delamination growth outside of the region imaged by XRCT. Figures 9(b) and (c) show the distribution of Mode of fracture causing delamination at 3.1mm-displacement. In the colorbar 0% corresponds to an opening fracture mode (Mode I) and 100% to a shearing fracture mode (Modes II and III, noted as Mode II in the figures).

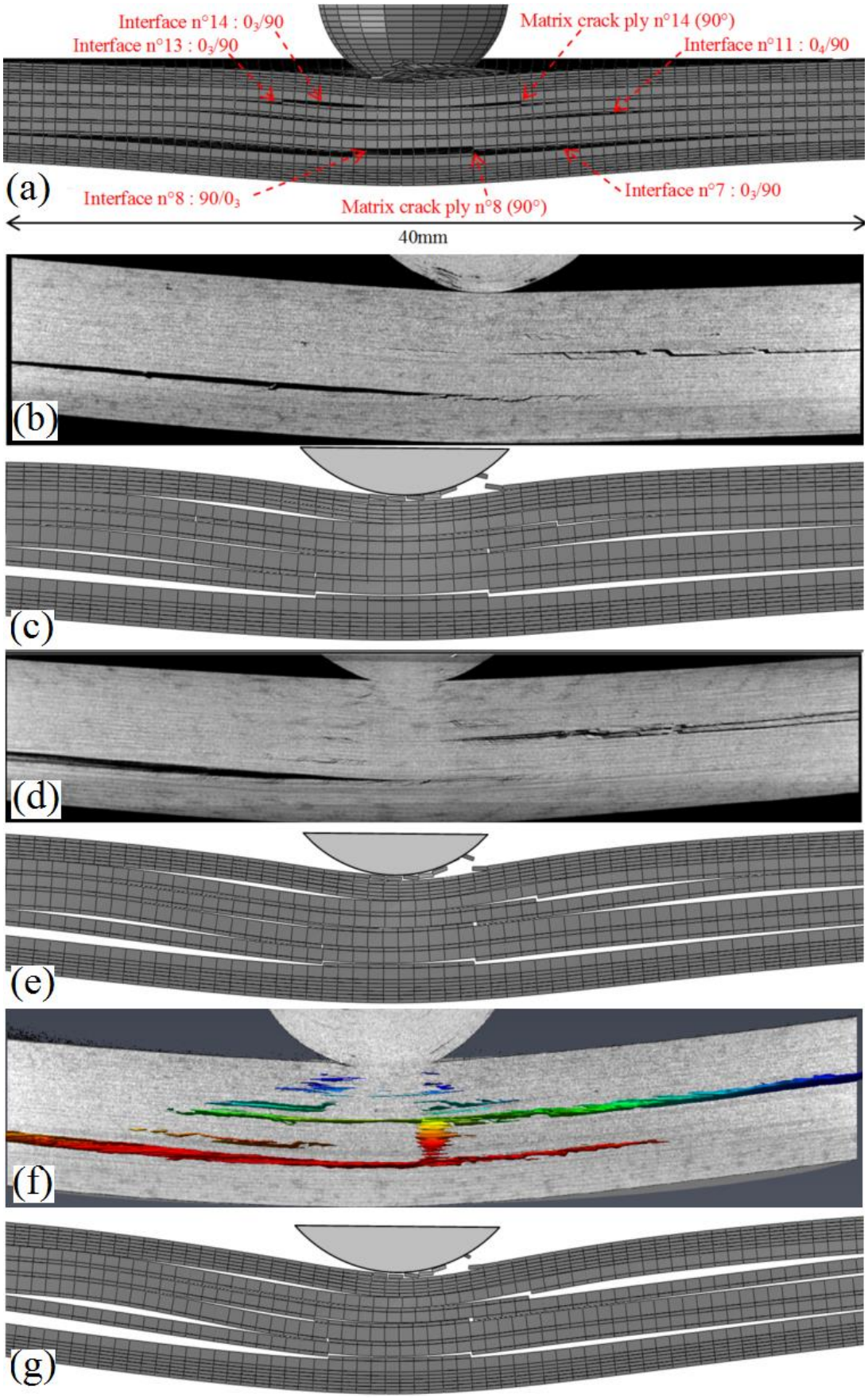

Figure 7: Damage in $[(\pm45)_3(0_3/90)_2/0_2]_S$ cross sectional view from front edge with laminate material present at (a) 2.5mm (b)-(c) 3.1mm, (d)-(e) 4.2mm and (f)-(g) 5.4mm. (a) is a DPFEA image and for (b)-(g) the XRCT experimental image is above and DPFEA image below.

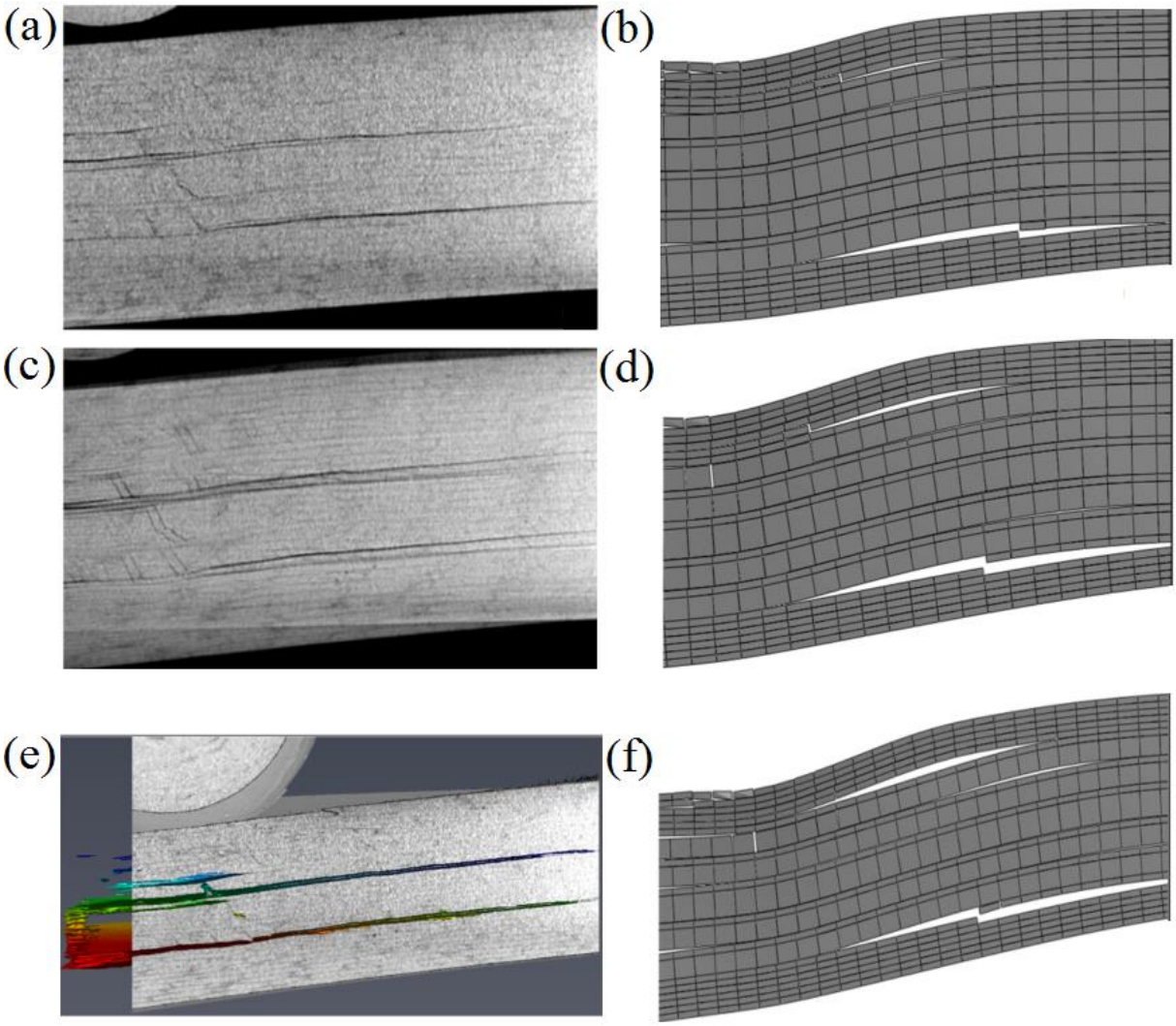

Figure 8: Damage in $[(\pm45)_3(0_3/90)_2/0_2]_S$ cross sectional view from side edge with laminate material present at (a),(b) 3.1mm, (c),(d) 4.2mm and (e),(f) 5.4mm (experiment left and model right).

6. DISCUSSION

In Fig. 6 DPFEA results for simply supported curved boundary, show good correlation with the experiment until 2.3mm displacement. After this point, the model shows a load drop and a plateau at 6.5kN. It believed the inaccurate response of the model is a consequence of (i) the difference in stiffness between experimental and numerical boundary conditions; (ii) a tightening force being imposed vertically on the boundary in the experiment but not in the numerical model; (iii) the effect of compression on matrix cracking and delamination not being taken into account in the DPFEA; (iv) the flexibility of the indenter not being captured – in the experiment the indenter is made of CFRP and displayed some cracking. To remove issue with (i) the numerical model of the boundary conditions will be improved in future work. To confirm that (ii) has an effect a clamped curved boundary was simulated, see Fig. 6. The clamped case shows an increasing load even after the load drop which is more consistent with the experiment. However, the clamped boundary is too stiff in comparison to the experiment. Hence all comparisons made with experiments are made using the simply supported boundary conditions. (iii) and (iv) will be addressed in future work.

A comparison of DPFEA and experimental results in Figs. 7 and 8 indicates there are discrepancies in the through thickness position of delamination growth. However, it is still interesting to understand the damage progression features captured by the DPFEA.

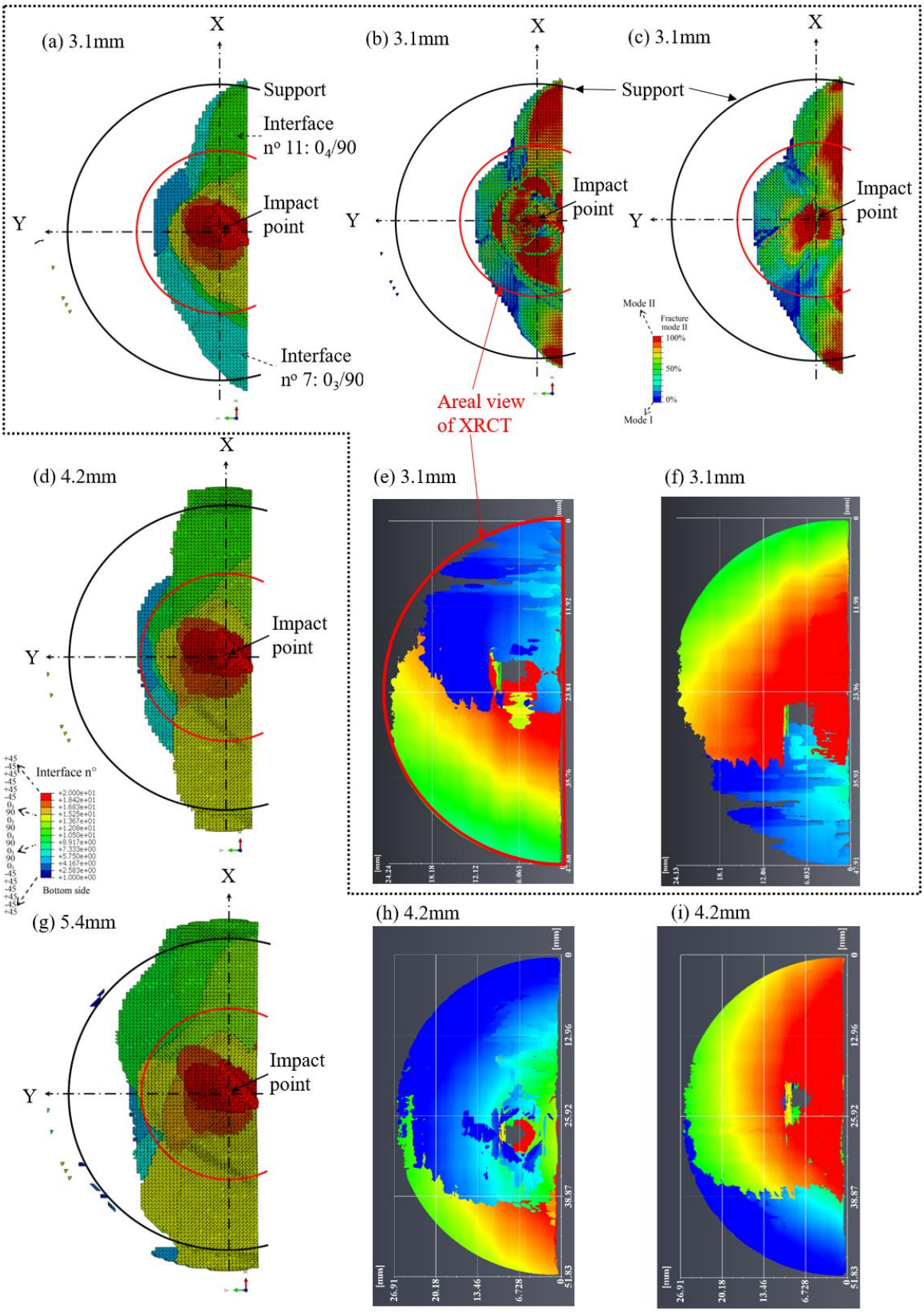

Figure 9: DPFEA Plan view of damage from the impact surface at an indentation of (a) 3.1mm, (d) 4.2mm and (e) 5.4mm. DPFEA in-plane distribution of Mode of fracture at 3.1mm viewed from (b) the impacted surface and (c) the non-impacted surface. Delamination extent viewed from the impact and non-impact surfaces at 3.1mm ((e) and (f) respectively) and 4.2mm ((e) and (f) respectively).

Figure 7(a) shows the damage in the plate seen from the free edge just after the load drop at 2.5mm-displacement. Before the load drop, the damage is small and consists of small matrix cracks and delaminations which are located just below the indenter and practically invisible from the free edge. At the load drop, a coupling between matrix cracking and delamination is observed. For example, two matrix cracks appear in ply n°8 at 90° and induce immediately delamination of the lower and upper interface; interfaces n°7, $0_3/90$ and n°8, $90/0_3$ respectively. Interface n°8 propagates in the direction of the lower adjacent 90° ply before being halted by the free edge. In contrast, interface n°7 propagates in the direction of the lower adjacent 0_3 ply and continues to propagate far from the impact point. The 0_3 ply group at interface n°7 is known to induce high interlaminar stress and explains the siginificant propagation at this interface. Delamination at interface n°7 is also clearly visible in Fig. 8 in both experimental and DPFEA images. A similar phenomenon is observed in the DPFEA at interface n°11 $0_4/90$ and interface n°13 $0_3/90$. However, these delaminations are not present in the experimental images in Fig. 8. As seen previously [28], Figs 7-9 show blocking of 0° plies contains damage to the core of the laminate potentially limiting the potential for delamination growth via sub-laminate buckling in a compression after impact scenario.

Delamination at interfaces n°7 and n°11 is particularly interesting because these delaminations are present in the experiment, contrast DPFEA and in-situ XRCT images in Figs. 7 and 8. However, the extent of propagation is larger in the DPFEA images. Additonally, although asymmetry is both experimentally and numerically obtained for interface n°11 (Figs 9(a), (d) and (g)), propagation at interface n°7, which is asymmetric in the experiment, is almost symmetrical in the DPFEA (Figs 7 and 9). This discrepancy in delamination at the 7th interface is believed to play a part in the discrepancy in average correlation of the DPFEA in Fig. 6.

Another clear discrepancy between the FEA and the experiment is the shape of the plate (Fig.7 and 8) under increasing indenter displacment. The shape numerically obtained shows a high plate curvature around the indenter, while the shape experimentally obtained is more flat. The excessive curvature observed by FEA is due to the excessive propagation of the delaminations. Indeed the delaminations cause sharp decreases in the bending stiffness of the plate and induce high curvature in the indenter zone. Due to the coupling between matrix cracking and delamination, it is difficult to conclude if this numerical discrepancy is due to excessive development of matrix cracks or of delamination. Moreover the boundary conditions also influence the development of damage and the discrepancy between experimental and DPFEA boundaries could explain the average correlation between experiment and model. This point will have to be more precisely considered in the future work.

Finally the model can be used to analyse the fracture mode of the delaminated interfaces (Fig. 9(b) and (c)). In impact tests, we observe classically a large opening fracture mode around the indenter and a larger shearing fracture mode far from the indenter [29]. This result is almost true in this case of near edge impact, except at the free edge. Indeed at the free edge, a largely shearing fracture mode is obtained, even far from the indenter zone.

7. CONCULSIONS AND FUTURE WORK

In this paper, a combined high fidelity Discrete Ply Finite Element Analysis (DPFEA) and quasi-static in-situ X-ray Computed Tomography (XRCT) approach is used to provide insight into the processes driving damage formation in near edge impact of a $[(\pm45)_3(0_3/90)_2/0_2]_S$ laminate. Damage is seen to be contained to the inner 50% of plies with delamination being driven by $0_n/90$ ply interfaces. Near and along the free edge delamination is predominantly driven by Mode II shearing fracture and delamination away from the free-edge has a significant contribution from Mode I fracture. DPFEA is able to capture the criticality of $0_n/90$ ply interfaces but displays significant delamination damage formation at $-45/0_3$ interfaces that is not present in the XRCT images. The indenter displacement at which significant delamination propagation occurs is also under predicted by the DPFEA. Both issues will be addressed in further work through improved boundary condition modelling and the inclusion of the effect of compression on the development of intra-ply fracture and delamination. Work will be extended to consider the effect of ply blocking on the progression of damage with increasing indentation through comparison of results with those for a $[(\pm45/0_2/90/0_2)_2/\pm45]_S$ sequence. Work will also be extended to consider impact and compression after impact under both near edge and central out-of-

plane of blocked ply sequences using DPFEA and in-situ XRCT. Work by Fletcher et al. [30] has shown that to correctly capture through thickness shear stresses >4 elements are required through the ply thickness. The effect of this will be explored as will the effect of free-edge stress concentrations.

REFERENCES

[1] C.S. Lopes, P.P. Camanho, Z. Gurdal, P. Maimi and E.V. Gonzalez, Low-velocity impact damage on dispersed stacking sequence laminates, Part II: Numerical simulations, *Composites Science and Technology,* **69**, 2009, pp. 937-947.

[2] D.J. Bull, L. Helfen, I. Sinclair, S.M. Spearing and T. Baumbach, A comparison of multi-scale 3D X-ray tomographic inspection techniques for assessing carbon fibre composite impact damage, *Composites Science and Technology,* **75**, 2013, pp. 55-61.

[3] S.R. Swanson, Limits of quasi-static solutions in impact of composite structures, *Composites Engineering,* **2**, 1992, pp. 261–267.

[4] H. Kaczmarek and S. Maison, Comparative ultrasonic analysis of damage in CFRP under static indentation and low-velocity impact, *Composites Science and Technology,* **51**, 1994, pp. 11-26.

[5] A.T. Nettles and M.J. Douglas, A Comparison of Quasi-Static Indentation to Low-Velocity Impact, *NASA Technical Publication NASA/TP-2000-210481,* 2000.

[6] B. Ostré, C. Bouvet, C. Minot and J. Aboissière, Edge impact modeling on stiffened composite structures, *Composite Structures,* **126**, 2015, pp. 314-328.

[7] Bolotin and V. Vladimir, Delaminations in composite structures: its origin, buckling, growth and stability, *Composites Part B: Engineering,* **27**, 1996, pp. 129-145.

[8] C. Breen, F. Guild and M. Pavier, Impact damage to thick carbon fibre reinforced plastic composite laminates, *Journal of materials science,* **41**, 2006, pp. 6718-6724.

[9] A. Malhotra, F.J. Guild, and M.J. Pavier, Edge impact to composite laminates: experiments and simulations, *Journal of materials science,* **43**, 2008, pp. 6661-6667.

[10] D. Liu, Impact-induced delamination – A view of bending stiffness mismatching, *Journal of composite materials,* **22**, 1988, pp. 674-692.

[11] R. Olsson, Closed form prediction of peak load and delamination onset under small mass impact, *Composite Structures,* **59**, 2003, pp. 341-349.

[12] R. Olsson, M.V. Donadon and B.G. Falzon, Delamination threshold load for dynamic impact on plates, *International Journal of Solids and Structures,* **43**, 2006, pp. 3124-3141.

[13] D. Liu and X. Li, An overall view of laminate theories based on displacement hypothesis, *Journal of composite materials,* **30**, 1996, pp. 1539-1561.

[14] M.O.W. Richardson, and M.J. Wisheart, Review of low-velocity impact properties of composite materials, *Composites Part A: Applied Science and Manufacturing,* **27**, 1996, pp. 1123-1131.

[15] C. Kassapoglou, *Modeling the Effect of Damage in Composite Structures: Simplified Approaches*, John Wiley & Sons, 2015.

[16] J. Serra, C. Bouvet, B. Castanié and C. Petiot. Scaling effect in notched composites: the discrete ply model approach, *Composite Structures,* **148**, 2016, pp. 127-143.

[17] B. Ostré, C. Bouvet, C. Minot and J. Aboissière, Finite Element analysis of CFRP laminates subjected to compression after edge impact, *Composite Structures,* **153**, 2016, pp. 478-489

[18] V. Achard, C. Bouvet, B. Castanié and C. Chirol, Discrete ply modelling of open hole tensile tests. *Composite Structures,* **113**, 2014, pp. 369-81.

[19] S. Rivallant, C. Bouvet and N. Hongkarnjanakul, Failure analysis of CFRP laminates subjected to compression after impact: FE simulation using discrete interface elements, *Composite Part A,* **55**, 2013, pp. 83-93

[20] N. Li and P.H. Chen, Micro-macro FE modelling of damage evolution in laminated composite plates subjected to low velocity impact, *Composite Structures,* **147**, 2016, pp. 111-121.

[21] C. Bouvet, S. Rivallant, and J.J. Barrau, Low velocity impact modeling in composite laminates capturing permanent indentation, *Composites Science and Technology*, **72**, pp. 1977-1988, 2012.

[22] Z.P. Bazant and B.H. Oh, Progressive crack band theory for fracture of concrete, *Materials and Structures*, **16**, 1983, pp. 155-77.

[23] E. Cosserat and F. Cosserat, Théorie des corps déformables, Hermann et fils, 1909.

[24] N. Germain, Modélisation non locale de l'endommagement dans les structures composites, École Nationale Supérieure des Mines de Paris, 2006.

[25] O. Allix, P. Feissel, and P. Thévenet, A delay damage mesomodel of laminates under dynamic loading: basic aspects and identification issues, *Computers and Structures*, **81**, 2003, pp. 1177-1191

[26] L. Marcin, J.F. Maire, N. Carrère and E. Martin, Development of a macroscopic damage model for woven ceramic matrix composites, *International Journal of Damage Mechanics*, **20**, 2011, pp. 939-957.

[27] H.B. Hellweg, Nonlinear failure simulation of thick composite structures, Imperial College of Science, Technology and Medicine, London, 1994.

[28] A. T. Rhead, S. Hua, and R. Butler, Damage resistance and damage tolerance of hybrid carbon-glass laminates, *Composite Part A*, **76**, 2015, pp. 224-232.

[29] C. Bouvet, N. Hongkarnjanakul, S. Rivallant and J.J. Barrau, *Dynamic failure of composite and sandwich structures*, chapter 8: Discrete impact modelling of inter- and intra-laminar failure in composites, Springer 2012.

[30] T. A. Fletcher, T. Kim, T. J. Dodwell, R. Butler, R. Scheichl, and R. Newley. Resin treatment of free edges to aid certification of through thickness laminate strength, *Composite Structures*, **146**, 2016, pp. 26-33.